Article

Dynamic Characteristics of Bidirectional Misaligned Marine Water-Lubricated Bearings Considering Turbulence, Surface Roughness and Bush Deformation

Ziqi Chen [1], Ji Wang [1,2,3,*], Rui Li [1,3] and Yujun Liu [1,2,3]

[1] School of Naval Architecture and Ocean Engineering, Dalian University of Technology, Dalian 116024, China
[2] State Key Laboratory of Structural Analysis for Industrial Equipment, Dalian 116024, China
[3] Dalian Key Laboratory of Advanced Shipbuilding Technology, Dalian 116024, China
* Correspondence: wangji@dlut.edu.cn; Tel.: +86-155-4268-1106

Abstract: The marine water-lubricated bearing's (WLBs) dynamic properties are essential for ensuring the shaft system's operational dependability. The coupled model of mixed lubrication and turbulence under the impact of bidirectional misalignment is proposed in this research, and the perturbation equations of marine WLBs with 32 coefficients are derived. The finite difference method (FDM) is used to solve the steady-state and perturbation equations, and the impacts of turbulence, bearing bush deformation, surface roughness, and bidirectional shaft misalignment on the dynamic characteristics of the WLBs are systematically investigated. The results reveal that under mixed lubrication, surface roughness and the turbulence effect can both greatly improve the stiffness and damping of the bearings, but that there is a threshold phenomenon for the turbulence effect's influence on these properties. Neglecting the elastic deformation of the bush may lead to an overestimation of the bearings' stiffness and damping, causing substantial inaccuracies in conditions of heavy load or declined Young's modulus. The 32 coefficients of the WLB exhibit considerable variation with the misalignment angle; hence, a more comprehensive dynamic model should be developed for misaligned marine WLBs. The study's findings provide valuable insights for rotor dynamics research and optimal design of lubrication performance in marine WLBs.

Keywords: marine water-lubricated bearing; turbulence; mixed lubrication; bearing bush deformation; bidirectional misalignment; dynamic characteristics

1. Introduction

Better lubrication performance of marine WLBs is beneficial for enhancing the operating safety and dependability of the ship propulsion shaft system [1,2]. The WLB system is commonly used in maritime stern bearings due to its superior performance and benefits over oil-lubricated bearings, including energy efficiency, environmental sustainability, and reduced noise levels [3,4]. However, there are specific problems to consider: (1) Because water has a significantly lower viscosity than mineral oil, WLB exhibits smaller water film thickness under the same load condition, which is of the same order of magnitude as the bearing surface roughness, and the WLB is more prone to a mixed lubrication state under heavy load conditions [5]. (2) The WLB is typically misaligned in both vertical and

horizontal directions due to the propeller's self-weight and the uneven lateral forces generated during operation [6]; (3) The large diameter of the ship's propulsion shaft system causes the bearing system to be subjected to turbulent lubrication conditions, exacerbated by a high relative slip velocity and a low viscosity fluid; (4) The marine WLB bush has a low Young's modulus, making it susceptible to wear and distortion, which can lead to anomalous vibration and noise emission [7]. A more comprehensive model is essential to better understand the complex dynamic behavior of the ship propulsion shaft system, as the current WLB dynamic model seldom integrates these features.

Extensive research has been conducted on the topic of mixed lubrication. When the bearing is in mixed lubrication, the minimum film thickness is typically of the same order of magnitude as the surface roughness. To characterize the impact of roughness parameters on lubrication performance, Patir et al. [8] established the average Reynolds equation taking surface roughness into account and introduced the flow factor and shear factor based on the traditional Reynolds equation. A GW contact model for two rough surfaces in contact was subsequently presented by Greenwood et al. [9] based on a statistical model. Liang et al. [10] proposed a deterministic model to study the influence of surface roughness on the mixed lubrication performance of thrust bearings. Wang et al. [11] pointed out that surface roughness and elastic deformation substantially affect the lubrication performance of bearings. He et al. [12] developed a mixed lubrication model for ship stern bearings, incorporating the effects of cavitation, and investigated the influence of bending deformation on the transition of lubrication states. Xie et al. [13] investigated the regulation of the asperity contact load ratio of WLB when transitioning from mixed lubrication to hydrodynamic lubrication and established a coupling relationship that was later validated by experiment. Charamis et al. [14] studied the influence of surface roughness and thermal effects on the lubrication performance of marine WLBs. Xiang et al. [15] presented a profile modification method to improve the contact and wear behavior of WLB under mixed lubrication and discussed the effect of asperity contact on adhesive wear behavior [16]. Zhao et al. [17] analyzed the effects of local wear and surface roughness on the performance of mixed lubrication in ship stern bearings. It is evident that the aforementioned studies typically ignored the turbulence effect and assumed laminar flow to exist inside the bearings.

A number of scholars have conducted relevant studies on the influence of turbulence on bearing lubrication performance. According to Wang's research [18], turbulence and thermal factors have a significant effect on the high-speed WLB's lubrication performance. Du et al. [19] investigated the lubrication properties of WLB under high-speed situations using four various mathematical models of turbulent lubrication. Lv et al. [20] investigated the effect of surface roughness, transient shock load, and turbulence on the mixed lubrication properties of bearings. Liu et al. [21] designed a high-speed WLB test rig to investigate the effect of turbulence on WLB at various speeds. Qiao et al. [22] employed a numerical method to investigate the influence of turbulence on the mixed lubrication performance of water-lubricated rubber bearings, demonstrating that turbulence can enhance bearing capacity while simultaneously diminishing contact load. However, the aforementioned research tends to ignore the effect of bearing misalignment.

The stern bearing is commonly misaligned because of the propeller's cantilever effect, and existing research has shown that this misalignment significantly affects the bearing's lubrication performance. Sun et al. [23] developed the film thickness equation of bearings under misalignment conditions to study the influence of various misalignment angles and eccentricities on the oil film pressure, bearing capacity, attitude angle, and friction coefficient. Liu et al. [24] developed a computational model of a ship's stern bearing with a bidirectional misalignment and investigated the impact on the dynamic properties. According to Lv's research [25], shaft misalignment significantly decreases the bearing

capacity and impairs the tribological performance of the bearings. Yang et al. [26] investigated the mixed lubrication and transient wear behavior of misaligned WLB. Xie et al. [27] examined the impact of misalignment on WLB lubrication performance and state transition.

More researchers have recently begun to focus on the impact of numerous parameters on the dynamic properties of bearings. Liang et al. [28] investigated the effect of disturbance amplitude on the stiffness coefficient of WLB using the CFD approach. Zhou et al. [29] examined the effect of groove number and structural parameters on the stiffness and damping properties of water-lubricated rubber bearings. Wang et al. [30] investigated the influence of bearing misalignment angle on the static and dynamic properties. Xiang et al. [31] investigated the dynamic characteristics of WLB under asperity contact considering different radial clearances, rubber thicknesses, and elastic moduli. Feng et al. [32] established a THD model to study the impact of thermal effects and turbulence on the dynamic properties of bearings. Ouyang et al. [33] conducted experimental studies of the dynamic characteristics of a ship's stern bearing, revealing that the bending deformation of the journal significantly increased the local dynamic characteristic coefficients of the bearing, particularly the stiffness coefficient. However, most of the current bearing dynamic studies are simplified eight-factor models that ignore the effect of journal misalignment and cannot accurately reveal the actual working status of marine WLBs. There is also a lack of a coupled model that takes into account turbulence and mixed lubrication to study the influence of complex factors on the dynamic characteristics of marine WLBs.

This study provided a mixed lubrication model for maritime WLBs that incorporated the effects of turbulence. Furthermore, the equation for water film thickness under bidirectional misalignment was developed, and the perturbation equation with 32 coefficients was derived and solved utilizing the FDM. The impacts of surface roughness, turbulence effect, bearing bush deformation, and bidirectional misalignment angle on the stiffness and damping properties of marine WLBs are systematically investigated.

2. Mathematical Model

2.1. The Generalized Average Reynolds Equation

Figure 1 illustrates the schematic structure of the WLB under mixed lubrication conditions, wherein asperity contact occurs around the location of minimal film thickness during operation at low speed and heavy load conditions. To account for the turbulence effect, a turbulence factor was incorporated based on the average Reynolds equation, and the generalized average Reynolds equation is presented in Equation (1). It should be noted that when the flow regime is laminar, the equation can be simplified to the conventional average Reynolds equation, which may be further simplified to the basic Reynolds equation if the impact of roughness is also neglected. As a result, the generalized average Reynolds equation provides a broader spectrum of applications [20,22].

$$\frac{\partial}{\partial x}\left(\phi_x \frac{h^3}{G_x \mu}\frac{\partial p}{\partial x}\right) + \frac{\partial}{\partial z}\left(\phi_z \frac{h^3}{G_z \mu}\frac{\partial p}{\partial z}\right) = 6U\phi_c \frac{\partial h}{\partial x} + 6U\sigma \frac{\partial \phi_s}{\partial x} + 12\phi_c \frac{\partial h}{\partial t} \tag{1}$$

where x and z are the bearing circumferential and axial coordinates, respectively, ϕ_x and ϕ_z are the pressure flow factor, ϕ_c is the contact factor [34], ϕ_s is the shear flow factor, p is the water film pressure, h is the water film thickness, μ is the viscosity, U is the journal rotational speed, σ is the surface composite roughness, G_x and G_z are the turbulence factors in the Ng-Pan model [35], respectively, which can be calculated using the following equation:

$$\begin{cases} G_x = \left(1 + 0.00113\, Re^{0.9}\right) \\ G_z = \left(1 + 0.000358\, Re^{0.96}\right) \end{cases} \tag{2}$$

where the Reynolds number can be determined using the following equation:

$$Re = \begin{cases} 0 & Rel < Rec \\ \rho Uh / \mu & Rel > Rec \end{cases} \tag{3}$$

where ρ is the density and Rel is the local Reynolds number. The microclearance shear flow inside a journal bearing during stable conditions can be treated as a Taylor–Couette flow [36]; therefore, this study adopted the critical Reynolds number to define the critical transition value from laminar to turbulent flow. When $Rel < Rec$ it is the laminar flow, while $Rel > Rec$ is the turbulent flow. Rec is the critical Reynolds number, which can be calculated as $Rec = 41.1/\sqrt{c/r}$ [20,22], c is the radial clearance, and r is the bearing radius.
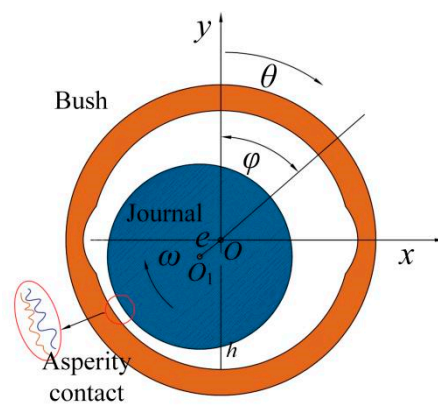
Figure 1. Schematic diagram of WLB.

2.2. Water Film Thickness Equation

The schematic of a misaligned journal is shown in Figure 2 The water film thickness is no longer uniformly distributed along the axial and circumferential directions, and the centre of the journal yields misalignment displacements Δx and Δy in each cross-section due to the misalignment angle in both directions, and the equation for the water film thickness at any cross-section can be expressed in terms of geometric gap and elastic deformation:

$$h(\theta,z) = c\left(1 + \varepsilon_0\right)\cos\left(\theta - \varphi\right) + \Delta x \cos\theta + \Delta y \sin\theta + \delta_E\left(\theta,z\right) \tag{4}$$

where c is the bearing radial clearance, ε_0 is the eccentricity ratio at the centre of the bearing, θ is the circumferential angle, z is the axial coordinate, φ is the attitude angle, δ_E is the bearing bush deformation, and Δx and Δy can be determined by the following equations:

$$\begin{cases} \Delta x = z\tan\gamma_y \approx z\gamma_y \\ \Delta y = z\tan\gamma_x \approx z\gamma_x \end{cases} \tag{5}$$

where γ_x is the journal misalignment angle around the x coordinate, γ_y is the journal misalignment angle around the y coordinate.
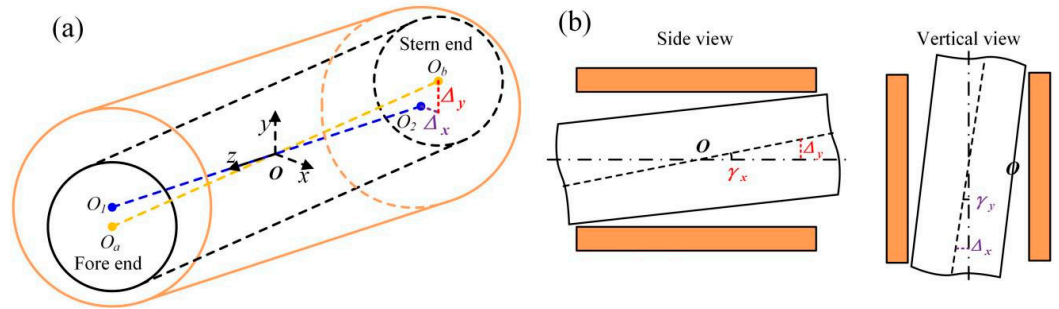
Figure 2. Schematic diagram of bidirectional misaligned WLB. (a): bidirectional misalignment; (b): projection of different coordinates.

Due to the small Young's modulus of the WLB bush, the deformation during operation can not be neglected, and this study employs the influence coefficient method (ICM) to compute the deformation of the bearing bush [11], as shown in the following equation:

$$\delta_E\left(\varphi_i, z_j\right) = \sum_\zeta \sum_\kappa G\left(\varphi_i, z_j, \varphi_\xi, z_\kappa\right)\left(p\left(\varphi_\xi, z_\kappa\right) + p_{asp}\left(\varphi_\xi, z_\kappa\right)\right) \tag{6}$$

where $G(\varphi_i, z_j, \varphi_\xi, z_k)$ is the matrix of influence coefficients indicating the amount of radial deformation at the node (φ_i, z_j) generated by the unit pressure at the node (φ_ξ, z_k), p is the water film pressure, p_{asp} is the contact pressure. G can be determined by ANSYS.

Figure 3 depicts the solution of bush elastic deformation. The finite element method (FEM) model is established by ANSYS Parametric Design Language (APDL) to calculate the G. To facilitate the calculation, the FEM nodes are coincident with FDM, and then the node numbers inside the bush are arranged in sequence. All the nodes outside the bush are subjected to fixed constraints, while the unit pressure is applied to the internal nodes in sequence, and the radial deformation of each node is solved to obtain the matrix of influence coefficients.
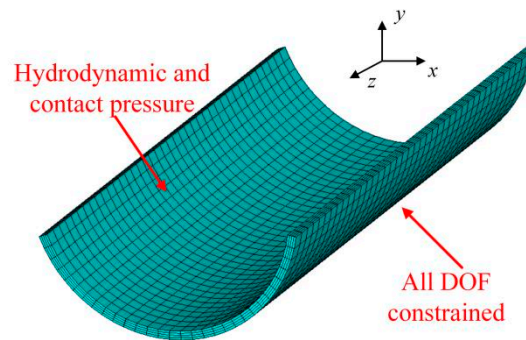
Figure 3. FEM for bearing bush deformation calculation.

2.3. Asperity Contact Model

The asperity contact pressure and the water film pressure share the bearing load in the mixed lubrication condition, and the G–W model is employed in this study to determine the contact pressure of the WLB in the mixed lubrication condition [9].

$$p_{asp} = K_{con} E^* F_{2.5}\left(H_d\right) \tag{7}$$

where p_{asp} is the contact pressure, E^* is the composite Young's modulus, $E^* = ((1 - v_J^2)/E_J + (1 - v_B^2)/E_B)^{-1}$, v is the Poisson's ratio, E is the Young's modulus of the material, J and B and represents the journal and the bearing, respectively, and K_{con} is the contact stiffness coefficient, which can be determined using the following equation:

$$K_{con} = 16\sqrt{2} / 15\pi (\sigma\beta\eta)^2 \sqrt{\frac{\sigma}{\beta}} \tag{8}$$

where σ is the composite roughness, β is the curvature radius of the asperities, and η is the density of the asperities.

$F_{2.5}(H_d)$ is a function related to the dimensionless film thickness ratio H_d [12]:

$$F_{2.5}(H_d) = \begin{cases} 4.4086 \times 10^{-5} (4 - H_d)^{6.804} & \text{if } H_d \leq 4 \\ 0 & \text{if } H_d > 4 \end{cases} \tag{9}$$

where $H_d = h/\sigma$ is the ratio of water film thickness to composite roughness.

2.4. Perturbation Equation

At present, the dynamic models of marine WLBs are commonly simplified, disregarding the impacts of surface roughness and turbulence. The mechanism of shaft bidirectional misalignment impact on the dynamic properties of bearing coupled translation and tilting degree of freedom (DOF) is yet unknown. In this study, a comprehensive 32 dynamic coefficient model incorporating the effects of multiple factors is proposed based on the generalized average Reynolds equation.

Assuming that h_0 is the water film's thickness in the equilibrium position, and the pressure is p_0, when they are perturbed, the dynamic properties of the water film can be determined by the perturbation pressure (the derivative of the pressure with respect to the displacement and velocity), the water film thickness and the pressure consisting of the steady-state term and the perturbation term, which can be obtained by performing a Taylor expansion of the terms and disregarding the higher order terms:

$$h = h_0 + \overline{x} \sin\theta + \overline{y} \cos\theta + z\overline{\gamma}_y \sin\theta + z\overline{\gamma}_x \cos\theta \tag{10}$$

$$p = p_0 + \overline{p}_{\overline{x}} \overline{x} + \overline{p}_{\overline{y}} \overline{y} + \overline{p}_{x'} x' + \overline{p}_{y'} y' + \overline{p}_{\overline{\gamma}_x} \overline{\gamma}_x + \overline{p}_{\overline{\gamma}_y} \overline{\gamma}_y + \overline{p}_{\gamma_{x'}} \gamma_x' + \overline{p}_{\gamma_{y'}} \gamma_y' \tag{11}$$

where $\overline{p}_{\overline{x}} = \frac{\partial p}{\partial \overline{x}}, \ \overline{p}_{\overline{y}} = \frac{\partial p}{\partial \overline{y}}, \ \overline{p}_{x'} = \frac{\partial p}{\partial x'}, \ \overline{p}_{y'} = \frac{\partial p}{\partial y'}, \ \overline{p}_{\gamma_x} = \frac{\partial p}{\partial \overline{\gamma}_x}, \ \overline{p}_{\gamma_y} = \frac{\partial p}{\partial \overline{\gamma}_y}, \ \overline{p}_{\gamma_{x'}} = \frac{\partial p}{\partial \gamma_{x'}}, \ \overline{p}_{\gamma_{y'}} = \frac{\partial p}{\partial \gamma_{y'}}$

Substituting the Taylor expansion equation for h and p to the generalized average Reynolds equation, then making it dimensionless, $H = h/c$, $P = p/6\mu rU/c^2$, $\lambda = 2z/L$, $\theta = x/r$, $H_d = h/\sigma$. The Reynolds equation for the unsteady state can be obtained, and the differential equations for each of the perturbation pressures can be obtained using the derivation:

$$\left[\frac{\partial}{\partial\theta}\left(\phi_x\frac{H^3}{G_x\mu}\frac{\partial}{\partial\theta}\right)+\left(\frac{D}{L}\right)^2\frac{\partial}{\partial\lambda}\left(\phi_z\frac{H^3}{G_z\mu}\frac{\partial}{\partial\lambda}\right)\right]\left[\overline{P}_\xi\right]=F_\xi\left(\xi=0,\overline{x},\overline{y},x',y',\gamma_x,\gamma_y,\gamma_x',\gamma_y'\right)$$

$$\begin{bmatrix}
F_0 = \phi_c\dfrac{\partial H_0}{\partial\theta}+\sigma\dfrac{\partial\phi_s}{\partial\theta}\\[2mm]
F_x = \phi_c\cos\theta-\dfrac{\partial}{\partial\theta}\left(\phi_x\dfrac{3H_0^2}{G_x\mu}\sin\theta\dfrac{\partial P}{\partial\theta}\right)-\left(\dfrac{D}{L}\right)^2\dfrac{\partial}{\partial\lambda}\left(\phi_z\dfrac{3H_0^2}{G_z\mu}\sin\theta\dfrac{\partial P}{\partial\lambda}\right)\\[2mm]
F_{x'} = 2\phi_c\sin\theta\\[2mm]
F_y = -\phi_c\sin\theta-\dfrac{\partial}{\partial\theta}\left(\phi_x\dfrac{3H_0^2}{G_x\mu}\cos\theta\dfrac{\partial P}{\partial\theta}\right)-\left(\dfrac{D}{L}\right)^2\dfrac{\partial}{\partial\lambda}\left(\phi_z\dfrac{3H_0^2}{G_z\mu}\cos\theta\dfrac{\partial P}{\partial\lambda}\right)\\[2mm]
F_{y'} = 2\phi_c\cos\theta\\[2mm]
F_{\gamma_x} = -\phi_c\lambda\sin\theta-\dfrac{\partial}{\partial\theta}\left(\phi_x\dfrac{3H_0^2}{G_x\mu}\lambda\cos\theta\dfrac{\partial P}{\partial\theta}\right)-\left(\dfrac{D}{L}\right)^2\dfrac{\partial}{\partial\lambda}\left(\phi_z\dfrac{3H_0^2}{G_z\mu}\lambda\cos\theta\dfrac{\partial P}{\partial\lambda}\right)\\[2mm]
F_{\gamma_x'} = 2\phi_c\lambda\cos\theta\\[2mm]
F_{\gamma_y} = \phi_c\lambda\cos\theta-\dfrac{\partial}{\partial\theta}\left(\phi_x\dfrac{3H_0^2}{G_x\mu}\lambda\sin\theta\dfrac{\partial P}{\partial\theta}\right)-\left(\dfrac{D}{L}\right)^2\dfrac{\partial}{\partial\lambda}\left(\phi_z\dfrac{3H_0^2}{G_z\mu}\lambda\sin\theta\dfrac{\partial P}{\partial\lambda}\right)\\[2mm]
F_{\gamma_y'} = 2\phi_c\lambda\sin\theta
\end{bmatrix}\tag{12}$$

where $\xi=\left(0,\overline{x},\overline{y},x',y',\gamma_x,\gamma_y,\gamma_x',\gamma_y'\right)$, the first formula represents the steady-state equation for stationary conditions, whereas the subsequent eight formulas denote the perturbation equations for the non-stationary conditions. By resolving the perturbation pressure and integrating it inside the water film region, 32 stiffness and damping coefficients can be derived as follows:

$$K=\begin{bmatrix}
\dfrac{K_{xx}}{k_1} & \dfrac{K_{xy}}{k_1} & \dfrac{K_{x\theta_x}}{k_3} & \dfrac{K_{x\theta_y}}{k_3}\\[2mm]
\dfrac{K_{yx}}{k_1} & \dfrac{K_{yy}}{k_1} & \dfrac{K_{y\theta_x}}{k_3} & \dfrac{K_{y\theta_y}}{k_3}\\[2mm]
\dfrac{K_{\theta_x x}}{k_2} & \dfrac{K_{\theta_x y}}{k_2} & \dfrac{K_{\theta_x\theta_x}}{k_4} & \dfrac{K_{\theta_x\theta_y}}{k_4}\\[2mm]
\dfrac{K_{\theta_y x}}{k_2} & \dfrac{K_{\theta_y y}}{k_2} & \dfrac{K_{\theta_y\theta_x}}{k_4} & \dfrac{K_{\theta_y\theta_y}}{k_4}
\end{bmatrix}=\iint\begin{Bmatrix}-\sin\theta\\-\cos\theta\\-\lambda\cos\theta\\\lambda\sin\theta\end{Bmatrix}\begin{Bmatrix}\overline{P}_{\overline{x}} & \overline{P}_{\overline{y}} & \overline{P}_{\overline{\gamma}_x} & \overline{P}_{\overline{\gamma}_y}\end{Bmatrix}\tag{13}$$

$$C=\begin{bmatrix}
\dfrac{C_{xx}}{c_1} & \dfrac{C_{xy}}{c_1} & \dfrac{C_{x\theta_y}}{c_3} & \dfrac{C_{x\theta_y}}{c_3}\\[2mm]
\dfrac{C_{yx}}{c_1} & \dfrac{C_{yy}}{c_1} & \dfrac{C_{y\theta_x}}{c_3} & \dfrac{C_{y\theta_y}}{c_3}\\[2mm]
\dfrac{C_{\theta_x x}}{c_2} & \dfrac{C_{\theta_x y}}{c_2} & \dfrac{C_{\theta_x\theta_x}}{c_4} & \dfrac{C_{\theta_x\theta_y}}{c_4}\\[2mm]
\dfrac{C_{\theta_y x}}{c_2} & \dfrac{C_{\theta_y y}}{c_2} & \dfrac{C_{\theta_y\theta_x}}{c_4} & \dfrac{C_{\theta_y\theta_y}}{c_4}
\end{bmatrix}=\iint\begin{Bmatrix}-\sin\theta\\-\cos\theta\\-\lambda\cos\theta\\\lambda\sin\theta\end{Bmatrix}\begin{Bmatrix}\overline{P}_{x'} & \overline{P}_{y'} & \overline{P}_{\gamma_x'} & \overline{P}_{\gamma_y'}\end{Bmatrix}\tag{14}$$

where k_1, k_2, k_3, k_4 are the dimensionless stiffness factors, corresponding to $3\mu ULr^2/c^3$, $3\mu UL^2r^2/2c^3$, $3\mu ULr^2/c^2$, $3\mu UL^2r^2/2c^2$, respectively. c_1, c_2, c_3, c_4 are the dimensionless coefficient factors, corresponding to $3\mu Lr^3/c^3$, $3\mu L^2r^3/2c^3$, $3\mu Lr^3/c^2$, $3\mu L^2r^3/2c^2$, respectively. K is the dimensionless stiffness coefficient matrix, while C is the dimensionless damping coefficient matrix, x and y are the translational direction, θ_x and θ_y are the tilting direction. To be specific, $K_{\theta_x x}$ represents the change in vertical moment due to horizontal translational displacement. $C_{\theta_y\theta_x}$ represents the change in horizontal

moment due to vertical angular velocity. It should be noted that the conventional 8 coefficients model exclusively accounts for translational stiffness and translational damping, disregarding the coupling effect of translational and tilting DOF.

2.5. Boundary Condition

The mass conservation boundary conditions can more accurately describe the cavitation phenomena inside the WLB, but they are often accompanied by a significant amount of time consumption. In order to ensure a higher solving efficiency, the Reynolds boundary conditions are used in this research:

$$
\begin{cases}
P(\theta,0) = P(\theta,2\pi) \\
P(\theta,\lambda = \pm 1) = 0 \\
P(\theta,\theta_0) = 0, \dfrac{\partial P}{\partial \theta_0} = 0
\end{cases}
\tag{15}
$$

Since it is difficult to determine the depth of the water line when the water-lubricated bearings are in operation, in this study, the boundary of the bearings is set at the ambient pressure. In the iteration process of the pressure, at that time $P < 0$, set $P = 0$. The location of the water film rupture can be determined during the iteration. The boundary conditions for the perturbation equations are related to the boundaries of the entire water film pressure region.

2.6. Convergence Principle

During the numerical simulation, the parameters, primarily the steady-state water film pressure, bearing bush deformation, attitude angle, and perturbation pressure, should be continuously modified to satisfy the convergence criterion.

The convergence principle of water film pressure is as follows:

$$
\frac{\sum\sum \left| P(i,j)^{new} - P(i,j)^{old} \right|}{\sum\sum \left| P(i,j)^{new} \right|} \leq 10^{-6}
\tag{16}
$$

The convergence principle of bearing bush deformation is as follows:

$$
\frac{\sum\sum \left| \delta_E(i,j)^{new} - \delta_E(i,j)^{old} \right|}{\sum\sum \left| \delta_E(i,j)^{new} \right|} \leq 10^{-6}
\tag{17}
$$

The convergence principle of attitude angle is as follows:

$$
\frac{\left| \varphi^{new} - \varphi^{old} \right|}{\left| \varphi^{new} \right|} \leq 10^{-4}
\tag{18}
$$

$$
\begin{cases}
W_x = -\iint\limits_{A} (p + p_{asp}) \sin\varphi \, dA \\
W_y = -\iint\limits_{A} (p + p_{asp}) \cos\varphi \, dA \\
\varphi = a\tan(W_x / W_y)
\end{cases}
\tag{19}
$$

where W_x and W_y are the component forces of the water film in the horizontal and vertical directions, respectively. p is the water film pressure and p_{asp} is the contact pressure.

The convergence principle of perturbation pressure is as follows:

$$\frac{\sum\sum\left|\overline{P}_\xi\left(i,j\right)^{new}-P_\xi\left(i,j\right)^{old}\right|}{\sum\sum\left|P_\xi\left(i,j\right)^{new}\right|}\leq10^{-6} \tag{20}$$

where $\xi=\overline{x},\overline{y},x',y',\gamma_x,\gamma_y,\gamma_x',\gamma_y'$.

3. Numerical Schemes and Model Validation

3.1. Numerical Simulation Flowchart

Figure 4 depicts the numerical simulation flowchart for this study. The numerical computation consists of two components: the steady-state equation and the perturbation equation. The FDM is used to discretely solve the generalized averaged Reynolds equation, then the successive over-relaxation (SOR) method is used to obtain the water film pressure, the elastic deformation of the bearing bush is calculated by ICM, and the water film thickness equation is continuously updated, and the attitude angle is adjusted using the secant method until it converges. The steady-state equations' water film pressure distribution and thickness distribution are utilized as inputs to the perturbation equations, and the 32 stiffness and damping coefficients of the WLB are finally derived. The computational domain's grid size is set to 720 × 60, which was shown to have a high convergence accuracy.
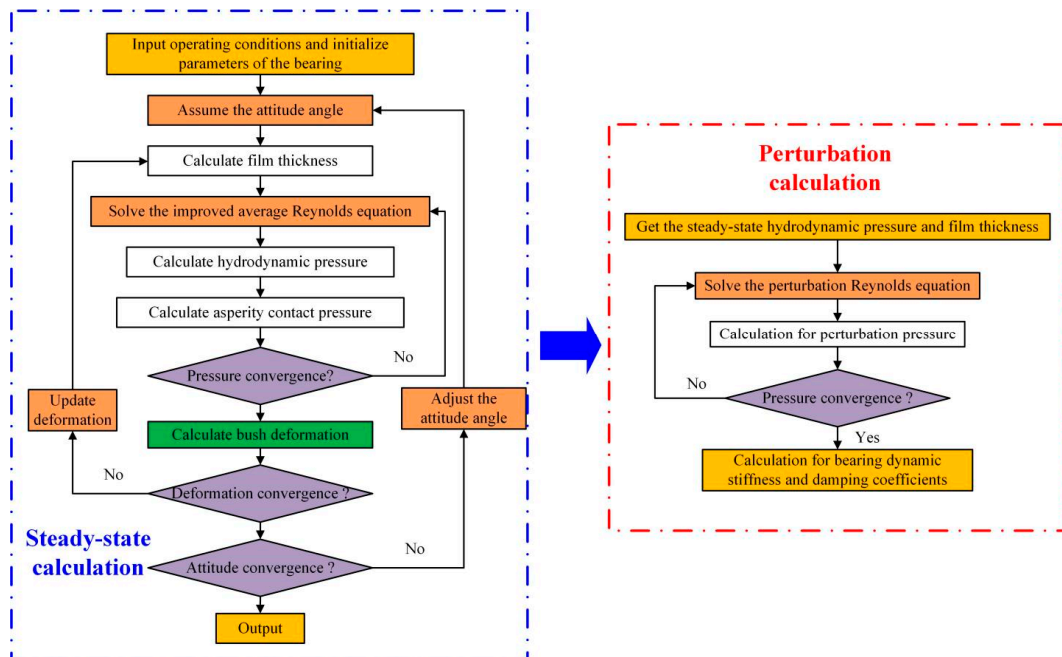
Figure 4. Flowchart of the numerical procedure.

3.2. Model Validation

To verify the accuracy of the calculation of the steady-state characteristics of WLB in this model, the calculation results of this model on the lubricant film pressure distribution are compared with the numerical calculation results of Dobrica et al. [36]. As shown in Figure 5a, the current model's results exhibit remarkable accuracy for both smooth and rough surface conditions, with a maximum pressure error of around 2%, enabling exact predictions of lubrication performance for various types of surface patterns. Table 1 illustrates the bearing parameters adopted by Dobrica et al.
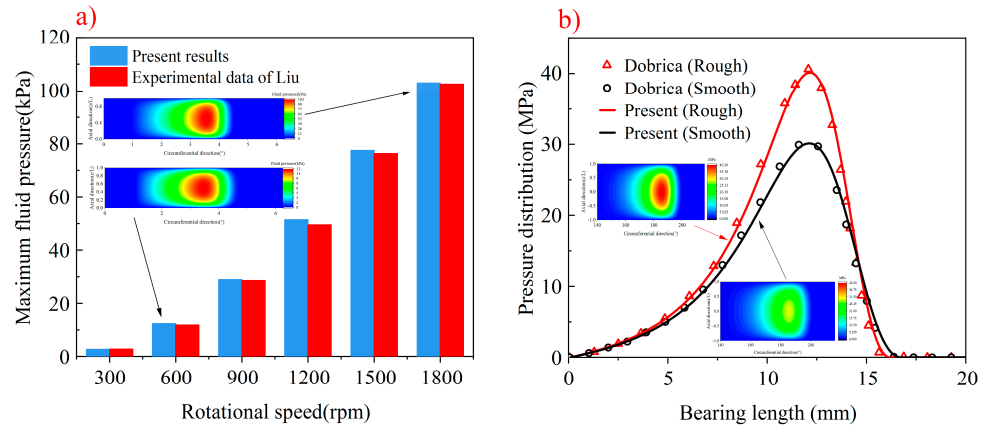
Figure 5. Comparison of present results with experimental data: (**a**) maximum fluid pressure considering turbulence effect; (**b**) fluid pressure distribution considering surface roughness.

Table 1. Bearing parameters of Dobrica.

Parameter	Value	Parameter	Value
Bearing diameter (D)	30 mm	Bearing Poisson's ratio (v_B)	0.33
Bearing length (L)	15 mm	Eccentricity ratio	0.945
Radial clearance (c)	0.022 mm	Viscosity (μ)	0.03 Pa·s
Rotational speed (n)	300 rpm	Roughness (σ)	0.4 μm
Bearing Young's modulus (E_B)	63 GPa	Surface orientation	1/9

To verify the accuracy of the turbulence model in this study, the numerical results are compared with the experimental results of Liu [21] and the numerical results of Qiao [22], and the parameters of the high-speed water-lubricated rubber bearing test rig are shown in Table 2. It is worth noting that the bush material utilized in Liu's experiment is rubber, and the impact of its elastic deformation is significant. Figure 5b presents a comparison of the maximum water film pressures at various rotational speeds and loads, which provides strong concordance and validates that the current model incorporates turbulence and bush deformation effects.

Table 2. Experimental parameters for Liu [20].

Parameter	Value	Parameter	Value
Bearing diameter (D)	120 mm	Load capacity(W)	0.09–3.12 kN
Bearing length (L)	480 mm	Rotational speed (n)	300–1800 rpm
Radial clearance (c)	0.4 mm	Bush material	Rubber
Viscosity (μ)	1.01×10^{-3} Pa·s	Bearing Young's modulus (E_B)	7.86 MPa
Bush thickness (l)	7.5 mm	Bearing Poisson's ratio (v_B)	0.47

To verify the validity of the mixed lubrication model in this study, the transient mixed lubrication results are compared with Mokhtar's experimental data [37]. As shown in Figure 6, it can be found that the present model is able to accurately predict the transient mixed lubrication behavior of the rotor during the start-up phase, which is closer to Cui's numerical results [38].
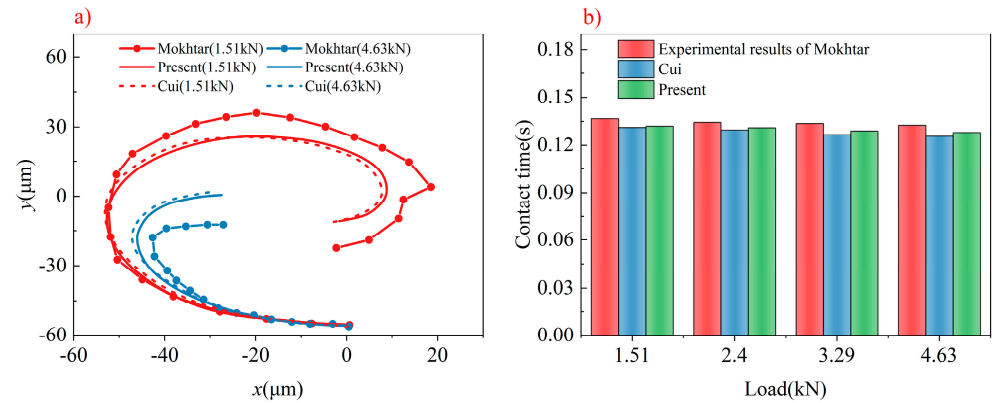
Figure 6. Verification of the accuracy of mixed lubrication modeling: (**a**) rotor orbit predicted by mixed lubrication model; (**b**) contact behavior.

To validate the accuracy of the dynamic characteristics calculation results in the present model, the numerical results are compared with those of Liu [39], who adopted a bearing with an L/D ratio of 2, a length of 80 mm and a radius clearance of 0.08 mm. It should be noted that the method adopted by Liu is the difference method, which is quite different from that in this research. Table 3 compares the tilting stiffness and damping coefficients under different eccentricity, and it can be seen that the calculation results of the two methods are reasonably close.

Table 3. Comparison of dimensionless coefficients calculated by difference method.

	ε	$K_{\theta_x\theta_x}$	$K_{\theta_x\theta_y}$	$K_{\theta_y\theta_x}$	$K_{\theta_y\theta_y}$	$C_{\theta_x\theta_x}$	$C_{\theta_x\theta_y}$	$C_{\theta_y\theta_x}$	$C_{\theta_y\theta_y}$
Liu	0.1	7.69×10^1	4.46×10^2	5.55×10^2	-1.38×10^2	4.42×10^2	5.71×10^1	-5.77×10^1	-5.64×10^2
Present	0.1	7.74×10^1	4.51×10^2	5.64×10^2	-1.40×10^2	4.46×10^2	5.86×10^1	-5.86×10^1	-5.73×10^2
Liu	0.5	7.39×10^2	1.07e3	4.32×10^2	-9.51×10^2	9.07×10^2	4.39×10^2	-4.41×10^2	-7.68×10^2
Present	0.5	7.47×10^2	1.09e3	4.36×10^2	-9.62×10^2	9.16×10^2	4.45×10^2	-4.45×10^2	-7.77×10^2
Liu	0.9	3.64×10^4	2.00×10^4	-7.05×10^3	-8.45×10^3	1.49×10^4	4.53×10^3	-4.57×10^3	-2.37×10^3
Present	0.9	3.56×10^4	2.04×10^4	-7.05×10^3	-8.58×10^3	1.51×10^4	4.58×10^3	-4.58×10^3	-2.46×10^3

4. Results and Discussion

The effects of surface roughness, turbulence, bearing bush deformation, and bidirectional misalignment on the stiffness and damping coefficients of marine WLBs have been investigated by adopting the model proposed in this study. The parameters of WLB adopted in this study are listed in Table 4.

Table 4. Parameters of WLB in this study.

Parameter	Value	Parameter	Value
Shaft radius (r)	224.6 mm	Asperity radius (β)	2 μm
Bearing radius (R)	225 mm	Asperity density (η)	2×10^{11}/m^2
Bush thickness (l)	15 mm	Journal material	45Cr
Bearing length (L)	990 mm	Bearing material	Thordon
Radial clearance (c)	0.4 mm	Viscosity (μ)	1.005×10^{-3} Pa·s
Rotational speed (n)	250 rpm	Dry friction	0.15
Journal Poisson's ratio (v_J)	0.3	Bearing roughness (σ_B)	1.6 μm
Bearing Poisson's ratio (v_B)	0.45	Journal roughness (σ_J)	1.2 μm
Journal Young's modulus (E_J)	210 GPa	Surface orientation (γ)	1
Bearing Young's modulus (E_B)	490 MPa	Wrap angle	150°

4.1. Effect of Surface Roughness

The effect of surface roughness on the dynamic characteristics of marine WLBs is investigated. When the WLB operates at low speeds and heavy loads, the influence of surface roughness is not negligible since the minimum nominal film thickness approaches the same order as the surface roughness and the bearings enter a mixed lubrication condition. The composite roughness range is 0–6 μm, where "0" indicates a smooth surface, the eccentricity ratio is 0.99, the rotational speed is 20 rpm, and the horizontal and vertical misalignment angles are both 0°.

Figure 7a–d depict the relationship between the stiffness coefficients of the WLB and surface roughness. The stiffness coefficients evidently increase with the increase in surface roughness. When surface roughness is minimal, mixed lubrication exerts a minor influence on the bearing stiffness coefficients, resulting in a small difference from a smooth surface. Nonetheless, as surface roughness increases, a significant increase in the stiffness coefficients is observed. When the surface roughness is increased from 0 to 6 μm, K_{xx}, K_{xy}, K_{yx}, K_{yy} increases by 24.14%, 19.08%, 16.13%, and 26.34%, respectively, whereas, $K_{\theta_x\theta_x}$, $K_{\theta_x\theta_y}$, $K_{\theta_y\theta_x}$, $K_{\theta_y\theta_y}$ increases by 26.57%, 17.19%, 18.97%, and 24.88%. The vertical translational stiffness coefficient K_{yy} and the horizontal tilting stiffness coefficient $K_{\theta_x\theta_x}$ are more sensitive to roughness variations. Upon comparing the magnitudes of the stiffness coefficients, it is evident that the coefficients in the vertical force direction K_{yy} and $K_{\theta_x\theta_x}$ are significantly greater than those in other directions, attributable to the direct correlation of the vertical force and the horizontal moment. Interestingly, these two stiffness coefficients vary non-linearly with roughness, although the other stiffness coefficients increase approximately linearly. The stiffness does not change significantly as the roughness increases. For instance, increasing the roughness from 5 μm to 6 μm, K_{yy} only raises it by 0.91%.

Figure 8a–d depict the variation of WLB damping coefficients with surface roughness. The damping coefficients vary similarly to the stiffness coefficients and both increase with surface roughness. It should be noted that when the roughness exceeds 3 μm, the cross-damping coefficients, C_{xy}, C_{yx}, and $C_{\theta_x\theta_y}$, $C_{\theta_y\theta_x}$ are no longer equal, and the difference gradually increases. C_{yy}, $C_{\theta_x\theta_x}$ and K_{yy}, $K_{\theta_x\theta_x}$ demonstrate a comparable trend, gradually stabilizing as the surface roughness increases, suggesting that roughness presents a constrained impact on the stiffness and damping coefficients. On the one hand, increasing the roughness reduces the thickness of the water film, hence enhancing its stiffness and damping properties. However, as the roughness further increases, the quantity of contact asperities and the contact area also increase, leading to a gradual convergence of the shear flow factor towards zero, hence diminishing the flow capacity of the water film. Furthermore, as the roughness continues to increase, the stiffness and damping coefficients of the water film progressively diminish.
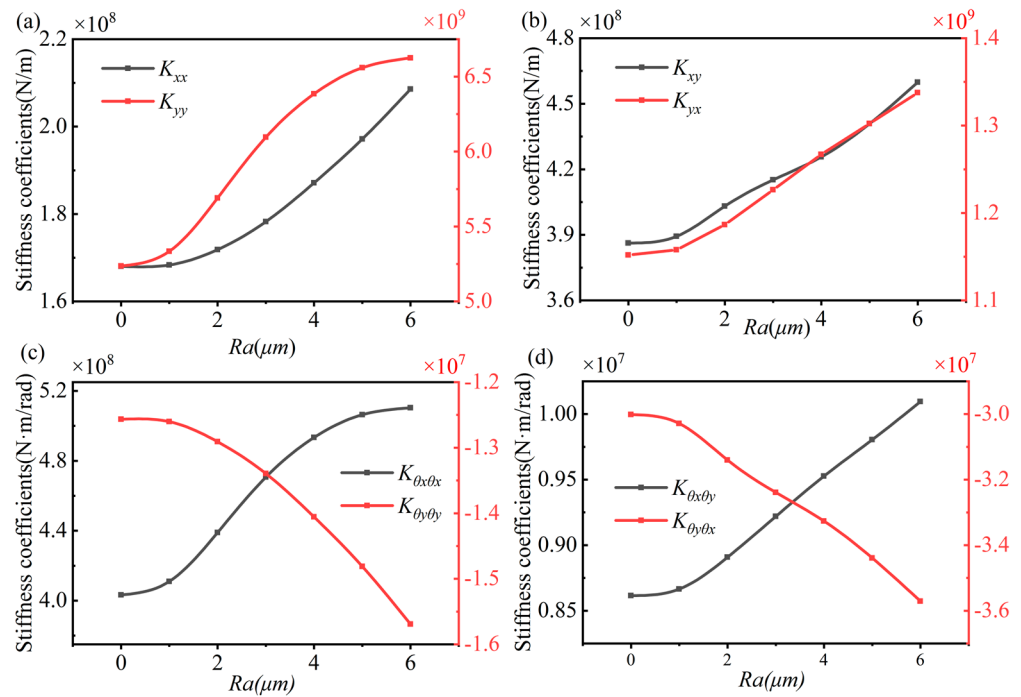
Figure 7. Effect of surface roughness on stiffness coefficients.
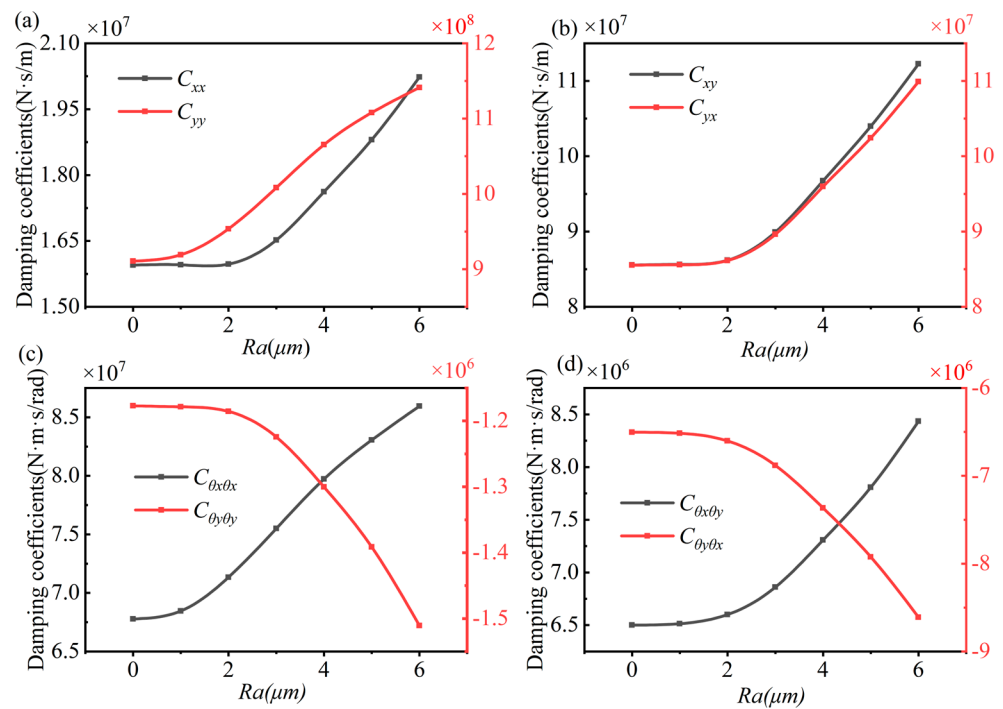
Figure 8. Effect of surface roughness on damping coefficients.

4.2. Effect of Turbulence

The effect of turbulence on the dynamic characteristics of marine WLBs is investigated. The bearing eccentricity ratio is 0.9, the composite roughness is 2 μm, the speed range is 15–300 rpm, and the horizontal and vertical misalignment angles are both 0°. It should be noted that under these conditions, the critical Reynolds number for turbulence is 975, which corresponds to a theoretical critical speed (TCS) of 55 rpm.

Figure 9a–d depict the variation of the stiffness coefficients of WLB at various speeds. At lower rotational speeds, there is essentially no difference between the turbulence model and the laminar flow model, but as the rotational speed increases, the discrepancy

grows and becomes almost linear. The turbulence effect can significantly enhance the stiffness coefficients of WLB compared to laminar flow. When the rotational speed is 300 rpm, compared with that of laminar flow, K_{xx}, K_{xy}, K_{yx}, K_{yy} increases by 46%, 36.93%, 19.09% and 14.05%, respectively. While $K_{\theta_x\theta_x}$, $K_{\theta_x\theta_y}$, $K_{\theta_y\theta_x}$, $K_{\theta_y\theta_y}$ increases by 12.10%, 17.54%, 39.41%, 45.23%, respectively, K_{xx} and $K_{\theta_y\theta_y}$ are more sensitive to turbulence effect.
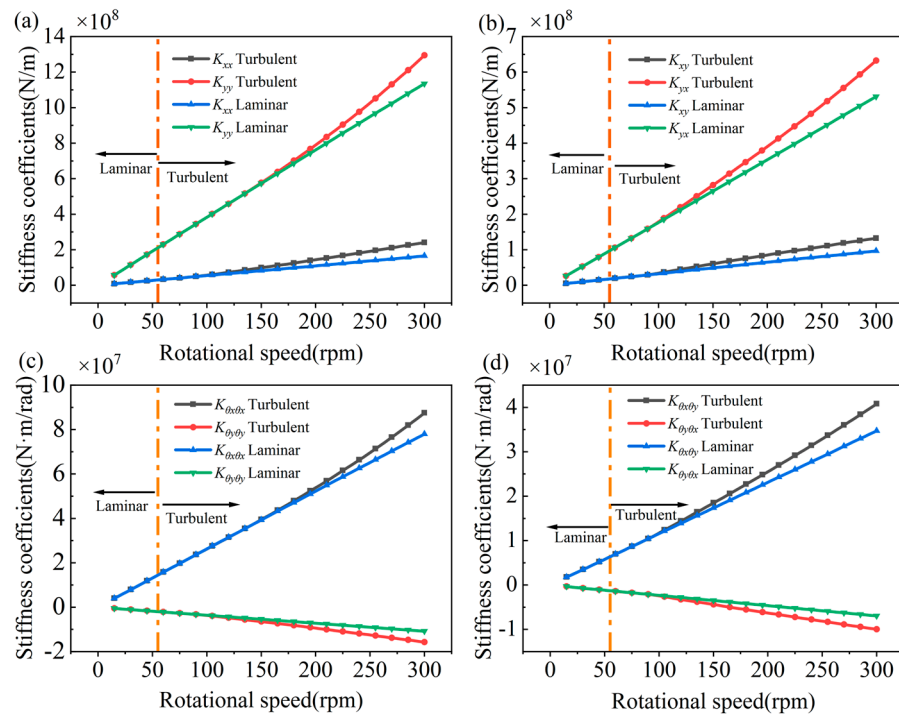
Figure 9. Effect of turbulence on stiffness coefficients at different rotational speeds.

An interesting threshold phenomenon can be observed; the actual critical speed (ACS—the speed at which turbulence affects the stiffness or damping coefficients to yield a deviation) is always higher than the TCS. However, this difference is not constant, it increases with larger values of the stiffness coefficients. The ACS of $K_{\theta_x\theta_x}$, $K_{\theta_x\theta_y}$, $K_{\theta_y\theta_x}$, $K_{\theta_y\theta_y}$ are 165 rpm, 120 rpm, 105 rpm, and 90 rpm, respectively. The convergence zone predominantly affects the dynamics of the WLB; at rotational speeds around the TCS, turbulence influences only the dispersion region and minimally affects the convergence region. As speed increases, the turbulence effect progressively extends to the convergence area, influencing the dynamic characteristics of the bearing. The convergence region is narrower with an increased stiffness coefficient, requiring a higher ACS.

Figure 10a–d depict the variation of the damping coefficients of WLB at various rotational speeds. The turbulence effect can dramatically enhance the damping coefficients of WLB, much like it did with the stiffness coefficients. More specifically, C_{xx} and $C_{\theta_y\theta_y}$ experience an increase of 61.46% and 57.89%, respectively, due to the turbulence effect. The damping coefficients of the WLB exhibit minimal variation with speed when the influence of turbulence is disregarded. Nevertheless, they exhibit non-linear changes and increase more rapidly at low rotational speeds. Additionally, the cross-damping coefficients C_{xy}, C_{yx}, and $C_{\theta_x\theta_y}$, $C_{\theta_y\theta_x}$ stay numerically equal and do not differ. The variation of the damping coefficients exhibits a similar threshold phenomenon.
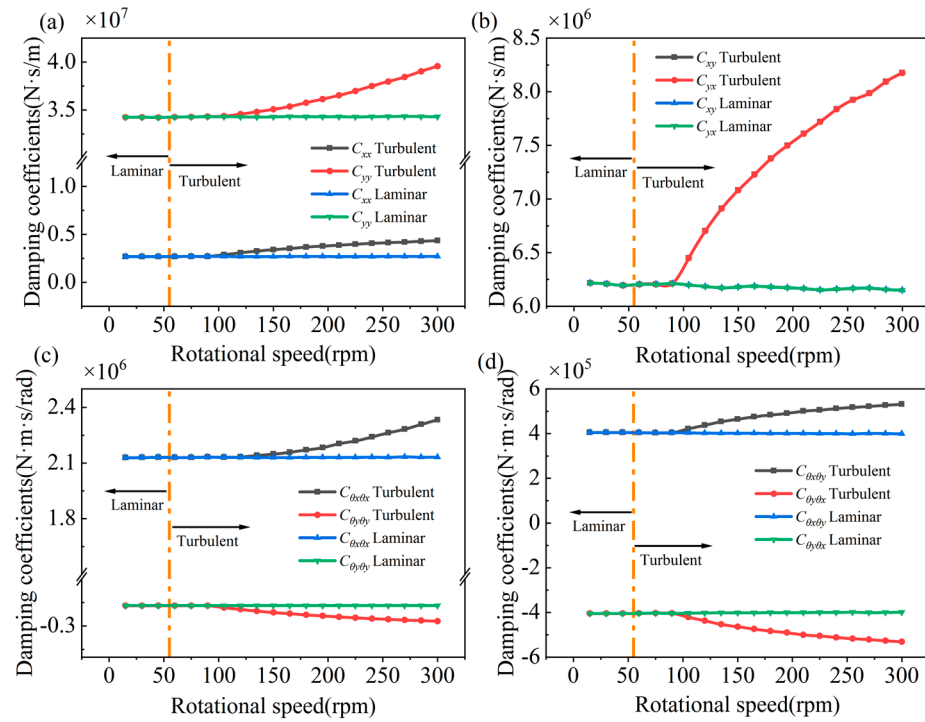
Figure 10. Effect of turbulence on damping coefficients at different rotational speeds.

4.3. Effect of Bearing Bush Deformation

The effect of bearing bush deformation on the dynamic characteristics of marine WLBs is investigated. The bearing eccentricity ratio range is 0.8–0.98, The Young's modulus of the bearing bush is taken as 200 MPa, 500 MPa, 800 MPa and rigid, respectively. The composite roughness is 2 μm, the rotational speed is 250 rpm, and the horizontal and vertical misalignment angles are both 0°.

Figure 11a–d depicts the variation of stiffness coefficient with eccentricity ratio for WLB at various Young's moduli. The stiffness coefficients of WLB with differing Young's modulus exhibit a non-linear increase when the eccentricity ratio rises, particularly when the eccentricity ratio exceeds 0.92, at which point the stiffness coefficients increase exponentially. The K_{yy} and $K_{\theta_x\theta_x}$ of rigid bush experienced the greatest variations, reaching 2.96×10^{10} N/m and 2.12e9 N/rad, respectively, at an eccentricity ratio of 0.98. The comparison indicates that the Young's modulus of the bush has no effect on the stiffness coefficients at smaller eccentricity ratios due to the lower water film pressure and deformation. When the eccentricity ratio exceeds 0.94, the stiffness coefficients show a considerable discrepancy, which increases with the eccentricity ratio. When the eccentricity ratio is 0.98, K_{yy} increases to 6.32×10^9 N/m, 1.10×10^{10} N/m, and 1.40×10^{10} N/m at the Young's modulus of 200 MPa, 500 MPa, and 800 MPa, respectively, and $K_{\theta_x\theta_x}$ increases to 4.95×10^8 N·m/rad, 8.49×10^8 N·m/rad, and 1.07×10^9 N·m/rad, respectively. Once bush deformation is disregarded, the discrepancy of K_{yy} amounts to 352.07%, 160.23%, and 104.56%, respectively, and the discrepancy of $K_{\theta_x\theta_x}$ amounts to 328.42%, 149.48%, and 97.53%, respectively. The deformation of the bearing bush significantly affects the stiffness coefficients of the WLB, particularly when the bush's Young's modulus is low or under heavy load conditions, where this discrepancy then becomes very pronounced.
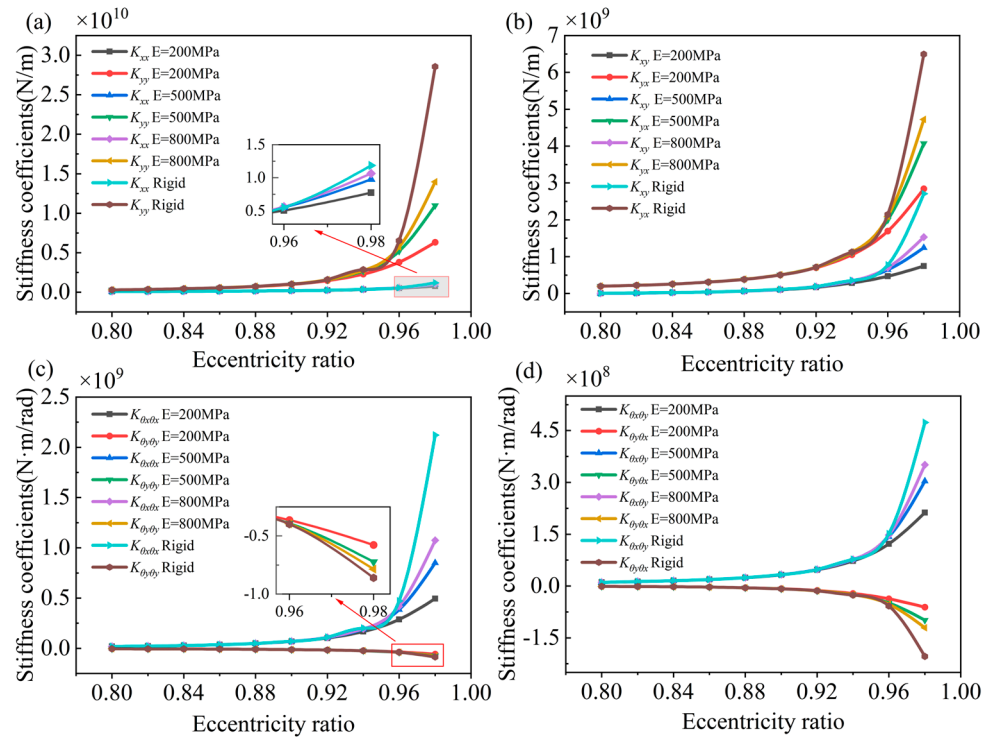
Figure 11. Effect of bush Young's modulus on stiffness coefficients for different eccentricity ratio.

Figure 12a–d depicts the variation of the damping coefficient with the eccentricity ratio for WLB at various Young's modulus. The damping coefficients rise non-linearly with an increase in the eccentricity ratio at varying bush Young's moduli, similar to the stiffness coefficients, and they are more noticeable when the eccentricity ratio is greater than 0.92. Neglecting the elastic deformation of the bush will lead to a substantial overestimation of the damping coefficients of the WLB. Upon comparing the variation rates of stiffness and damping coefficients in Figures 11 and 12, it is evident that the elastic deformation of the bush significantly affects the stiffness coefficients more than the damping coefficients. For instance, when the eccentricity ratio is 0.98, the discrepancy of C_{yy} in the Young's modulus of 200 MPa, 500 MPa, and 800 MPa amounts to 112.94%, 53.14%, and 33.52%, respectively, and the discrepancy of $C_{\theta_x\theta_x}$ amounts to 108.43%, 51.84%, and 32.63%, respectively, which are significantly less than K_{yy} and $K_{\theta_x\theta_x}$.
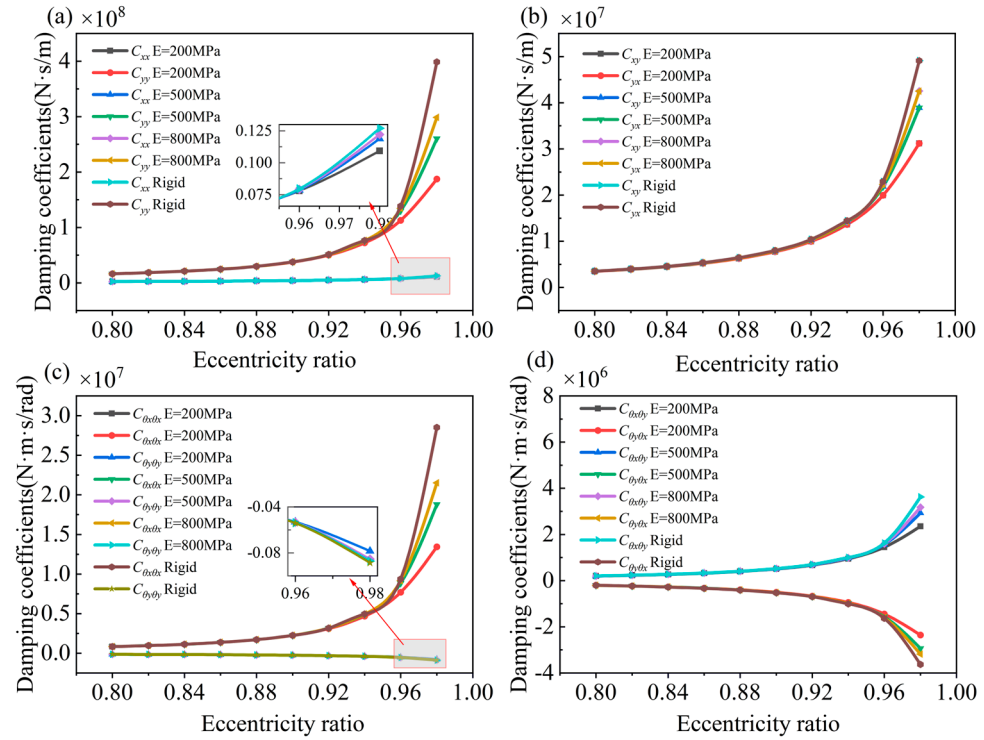
Figure 12. Effect of bush Young's modulus on damping coefficients for different eccentricity ratio.

4.4. Effect of Bidirectional Misalignment

The effect of bidirectional misalignment on the dynamic characteristics of marine WLBs is investigated. The WLB is typically misaligned in both vertical and horizontal directions due to the propeller's self-weight and the uneven lateral forces generated during operation. Classification societies normally demand that misalignment angles greater than 3.0×10^{-4} rad (0.3 mm/m) be addressed by inclined boring, hence the misalignment angle limit range is $\gamma = c/(2L)$ [24], which is 0–0.0116°. In this section, misalignment angles ranging from −0.008° to 0.008° in the horizontal and vertical directions are chosen for investigation, with an eccentricity ratio of 0.8 and a rotational speed of 250 rpm.

It should be emphasized that the misalignment angles in Sections 4.1–4.3 are assumed to be 0°, at which point the WLB's 16 coupled translational-tilting and tilting-translational stiffness and damping coefficients are nearly 0 and can be ignored when journal misalignment is disregarded.

Figure 13a–d depict the effect of various vertical misalignment angles γ_x on stiffness coefficients. The 16 stiffness coefficients increase with the misalignment angle; the larger the misalignment angle, the faster the change. The translational and tilting stiffness coefficients are symmetrically distributed as the vertical misalignment angle changes from -0.008° to 0.008°, but the coupled translational-tilting and tilting-translational stiffness coefficients are center-symmetric. This is because a misaligned journal influences the orientation of the moment to be altered instead of the direction of the joint force. When the vertical misalignment angle increases from 0 to 0.008°, K_{xx}, K_{xy}, K_{yx}, K_{yy} increase by 47.75%, 38.58%, 52.37% and 72.23%, respectively. While $K_{\theta_x\theta_x}$, $K_{\theta_x\theta_y}$, $K_{\theta_y\theta_x}$, $K_{\theta_y\theta_y}$ increase by 169.06%, 147.42%, 108.02% and 115.32%, respectively. The effect of vertical misalignment angle is more significant for K_{yy} and $K_{\theta_x\theta_x}$. Additional, $K_{x\theta_x}$, $K_{x\theta_y}$, $K_{y\theta_x}$, $K_{y\theta_y}$, $K_{\theta_x x}$, $K_{\theta_x y}$, $K_{\theta_y x}$ and $K_{\theta_y y}$ increase from 0 to 2.11×10^7 N/rad, 2.17×10^7 N/rad, 1.08×10^8 N/rad, 5.51×10^7 N/rad, 5.62×10^7 N·m/m, 1.11×10^8 N·m/m, -2.20×10^7 N·m/m, -2.16×10^7 N·m/m, respectively.

Figure 14a–d depict the effect of various horizontal misalignment angles γ_y on stiffness coefficients. The regularity of the 16 stiffness coefficients is comparable to that of vertical misalignment. As the horizontal misalignment angle increases from 0 to 0.008°, K_{xx}, K_{xy}, K_{yx}, K_{yy} increased by 23.30%, 19.12%, 16.60% and 18.09%, respectively. While $K_{\theta_x\theta_x}$, $K_{\theta_x\theta_y}$, $K_{\theta_y\theta_x}$, $K_{\theta_y\theta_y}$ increased by 36.75%, 47.86%, 58.54% and 67.39%, respectively. The effect of horizontal misalignment is more significant for K_{xx} and $K_{\theta_y\theta_y}$. Moreover, with the influence of horizontal misalignment, $K_{x\theta_x}$, $K_{x\theta_y}$, $K_{y\theta_x}$, $K_{y\theta_y}$, K_{θ_xx}, K_{θ_xy}, K_{θ_yx}, K_{θ_yy} increases from 0 to 1.46×10^7 N/rad, 1.71×10^7 N/rad, 3.56×10^7 N/rad, 2.93×10^7 N/rad, 2.95×10^7 N·m/m, 3.52×10^7 N·m/m, -1.73×10^7 N·m/m, -1.46×10^7 N·m/m, respectively.

The influence of horizontal misalignment on the 16 stiffness coefficients of the WLB is consistently less than that of vertical misalignment, as evidenced by the comparisons of stiffness coefficients across various misalignment directions in Figures 13 and 14. This suggests that the 16 stiffness coefficients of the WLB exhibit greater sensitivity to vertical misalignment. It is noteworthy that none of the eight associated translational-tilting stiffness and tilting-translational coefficients are zero for both horizontal and vertical misalignment angles. Consequently, neglecting the coupled translational-tilting and tilting-translational stiffness coefficients in the dynamic analysis of a misaligned shaft system could lead to a substantial inaccuracy for marine WLBs.
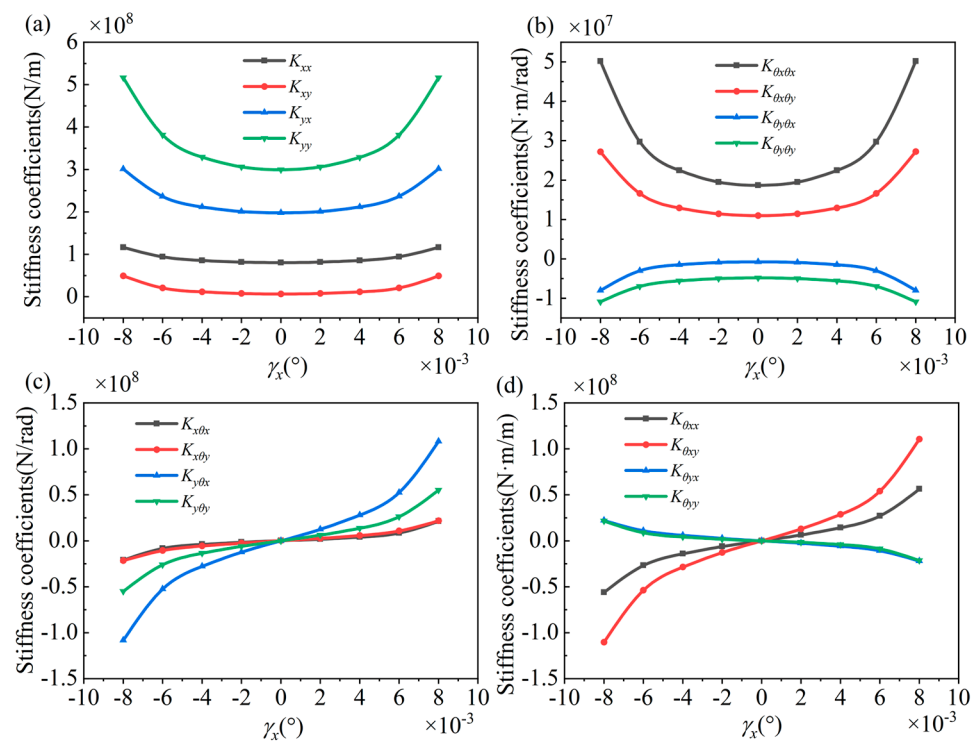
Figure 13. Effect of different vertical misalignment angles on stiffness coefficients.
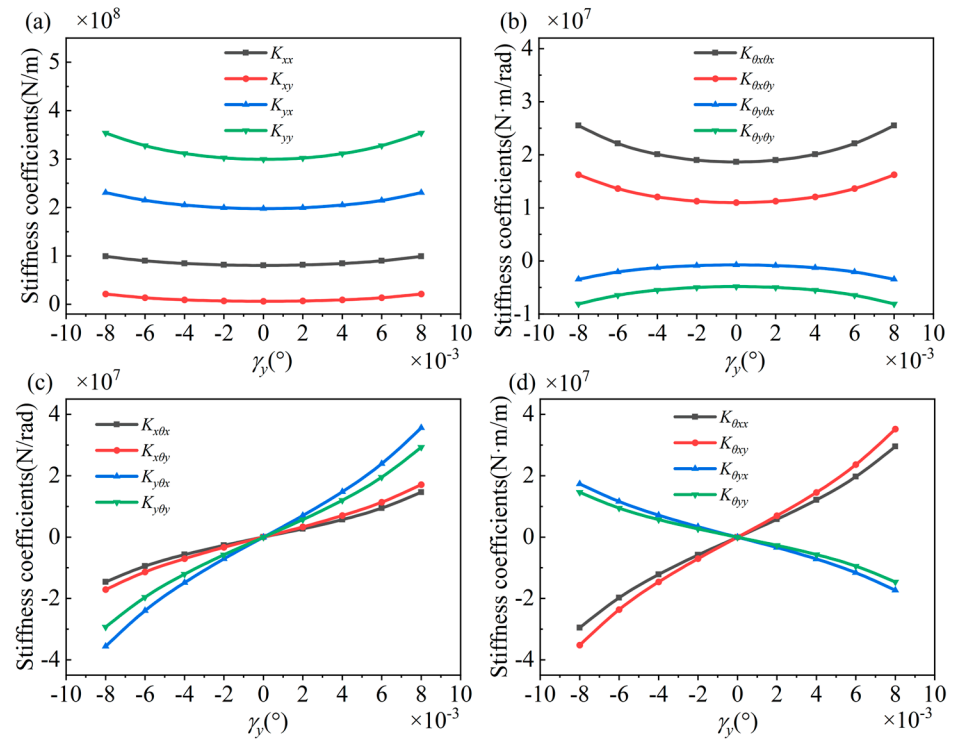
Figure 14. Effect of different horizontal misalignment angles on stiffness coefficients.

Figure 15a–d depict the effect of various vertical misalignment angle γ_x on the damping coefficients. The impact of vertical misalignment on the damping coefficient is comparable to that of stiffness coefficients, which change more quickly with increasing the misalignment angle. Around the vertical misalignment angle, the damping coefficients are also distributed symmetrically or center-symmetrically. As the vertical misalignment angle increases from 0° to 0.008°, C_{xx}, C_{yy}, $C_{\theta_x\theta_x}$, $C_{\theta_y\theta_y}$ increases to 2.86 × 10⁶ N·s/m, 2.20 × 10⁷ N·s/m, 1.62 × 10⁶ N·m·s/rad, −2.28 × 10⁵ N·m·s/rad, respectively. The cross-damping coefficients, for instance, C_{xy} and C_{yx}, $C_{\theta_x\theta_y}$ and $C_{\theta_y\theta_x}$, $C_{x\theta_x}$ and $C_{y\theta_y}$, $C_{\theta_x x}$ and $C_{\theta_y y}$ are still numerically identical, but all of them increase significantly from zero, which cannot be neglected.

Figure 16a–d depict the effect of various horizontal misalignment angles γ_y on the damping coefficients. The horizontal misalignment similarly affects damping coefficients as vertical misalignment, increasing with the misalignment angle and varying more rapidly with greater misalignment. The damping coefficients are symmetrically or center-symmetrically distributed around the zero-misalignment angle. With the increase in the misalignment angle, the cross-damping coefficients, such as C_{xy} and C_{yx}, $C_{\theta_x\theta_y}$ and $C_{\theta_y\theta_x}$, $C_{x\theta_x}$ and $C_{y\theta_y}$, $C_{\theta_x x}$ and $C_{\theta_y y}$ are still numerically identical, and gradually increase. When the vertical misalignment angle γ_x increased from 0° to 0.008°, C_{xx}, C_{yy}, $C_{\theta_x\theta_x}$, $C_{\theta_y\theta_y}$ increases to 2.78 × 10⁶ N·s/m, 1.78 × 10⁷ N·s/m, 1.02 × 10⁶ N·m·s/rad and −2.08 × 10⁵ N·m·s/rad, respectively.

By comparing the growth rate of damping coefficients with different misalignment angles in Figures 15 and 16, the vertical misalignment has a more significant impact on the damping coefficients of WLBs than horizontal misalignment. Comparing the growth rate of stiffness and damping coefficients, the effect of a misaligned journal on the stiffness coefficients is greater than on the damping coefficients. It is important to highlight that the eight coupled translational-tilting and tilting-translational damping coefficients are no longer zero for both horizontal and vertical misalignment angles and all exhibit significant variation. This indicates that for misaligned WLBs, the coupled translational-tilting and

tilting-translational stiffness and damping coefficients constitute a substantial aspect of the dynamic characteristics of the bearings and should be considered.
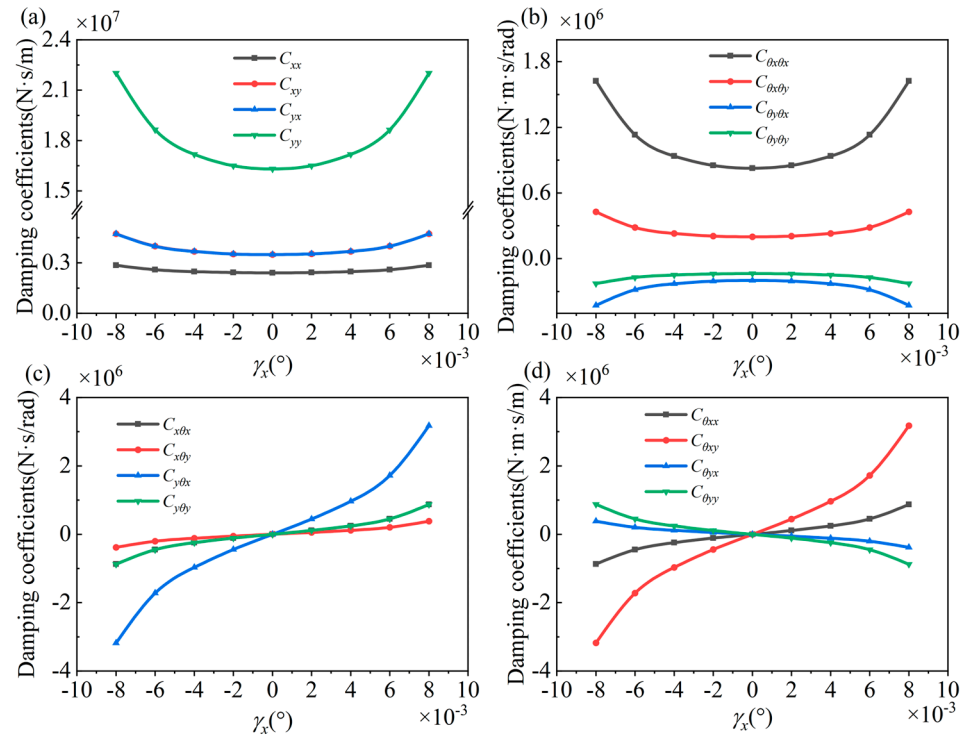
Figure 15. Effect of different vertical misalignment angles on damping coefficients.
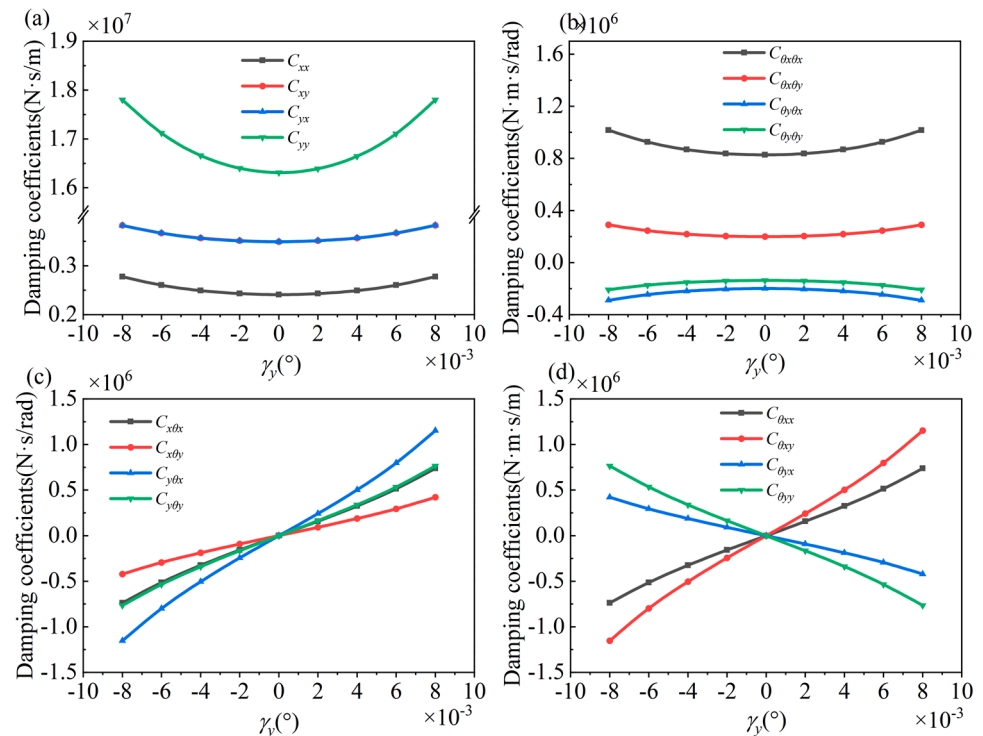
Figure 16. Effect of different horizontal misalignment angles on damping coefficients.

5. Conclusions

In this study, a coupled model with turbulence and mixed lubrication is proposed for marine WLBs with a large aspect ratio, and a perturbation equation with 32 coefficients is derived. The effect of surface roughness, turbulence effect, bearing bush deformation,

and horizontal and vertical misalignment on the dynamic characteristics of marine WLBs is systematically investigated. The main conclusions of this study are as follows:

(1) The stiffness and damping coefficients of marine WLBs in the mixed lubrication condition can be significantly enhanced by using an appropriate surface roughness; the K_{yy} and $K_{\theta_x\theta_x}$ are more sensitive to changes in roughness. However, the effect of surface roughness on enhancing the stiffness and damping of the water film gradually diminishes as it further increases.

(2) The turbulence effect can enhance the stiffness and damping coefficients of the WLB when the rotational speed exceeds the ACS. Larger stiffness or damping coefficients result in a higher ACS required for the threshold phenomenon to occur. While stiffness grows roughly linearly with speed, damping increases non-linearly and more quickly at lower speeds. K_{xx}, C_{xx} and $K_{\theta_y\theta_y}$, $C_{\theta_y\theta_y}$ are more affected by the turbulence effect.

(3) The impact of bearing bush deformation on the dynamic characteristics of WLBs cannot be ignored, particularly in cases of low Young's modulus or heavy loads, and the impact can be particularly significant, and the bush elastic deformation affects the stiffness coefficient of WLBs more than the damping coefficients.

(4) The 16 coupled translational-tilting and tilting-translational stiffness and damping coefficients are close to 0 and can be neglected when misalignment is not taken into account. For both horizontal and vertical misalignment, the WLB's 32 stiffness and damping coefficients dramatically change. The effect of vertical misalignment is more significant for K_{yy}, C_{yy}, and $K_{\theta_x\theta_x}$, $C_{\theta_x\theta_x}$, while the horizontal misalignment is more significant for K_{xx}, C_{xx} and $K_{\theta_y\theta_y}$, $C_{\theta_y\theta_y}$. A completed 32 coefficients dynamic model should be developed for misaligned marine WLBs.

(5) When designing marine WLBs, it is not recommended to use a relatively high surface roughness as this increases the possibility of the bearings entering a mixed lubrication condition and also reduces the stiffness and damping coefficient of the WLB, which is not conducive to stable operation. For heavy-loaded WLBs, the Young's modulus of the bush should be increased to improve the bearing's support performance. The misalignment effect during the actual operation of marine WLBs is inevitable, and the edge loading effect caused by it will have a significant impact on the dynamic characteristics of the bearing, and the misalignment angle should be controlled within 0.004°, and for horizontal misalignment, this range should be more stringent.

Conflicts of Interest: The authors declare no conflicts of interest.

Nomenclature

E	Young's modulus, MPa	K	stiffness coefficient matrix
H	dimensionless water film thickness	C	damping coefficient matrix
P	dimensionless water film pressure	β	curvature radius of the asperity, μm
W_x	horizontal load, kN	η	density of the asperity, 1/m³
W_y	vertical load, kN	θ	circumferential angle, rad
Re	Reynolds number	θ_0	film rupture angle, rad
Rec	critical Reynolds number	σ	surface composite roughness, μm
Rel	local Reynolds number	l	bush thickness, mm
U	rotational speed, m/s	λ	dimensionless axial coordinate
c	radial clearance, mm	μ	viscosity, Pa·s
e	eccentricity	ρ	density, kg/m³
h	water film thickness, μm	υ	Poisson's ratio
p	water film pressure, MPa	φ	attitude angle, rad
p_{ap}	contact pressure, MPa	γ_x	misalignment angle around x, °
r	bearing radius, mm	γ_y	misalignment angle around y, °
x	bearing circumferential coordinates, mm	δ_E	bearing bush deformation
y	bearing axial coordinates, mm	ε_0	eccentricity ratio
z	axial coordinate, mm	ϕ_x, ϕ_y	pressure flow factor
$\overline{P_\xi}$	dimensionless perturbation pressure	ϕ_c	contact factor
G_x, G_z	turbulence factors	ϕ_s	shear flow factor
H_d	film thickness ratio	$\Delta x, \Delta y$	misalignment displacements, mm
K_{con}	contact stiffness coefficient		

References

1. Huang, Q.; Yan, X. Impact factors on lubricant performance of stern bearing with misalignment angle induced by transverse vibration of shaft. *Ocean Eng.* **2020**, *216*, 108051.
2. Yang, H.; Li, J.; Li, X. Calculation of the dynamic characteristics of ship's aft stern tube bearing considering journal deflection. *Pol Marit Res.* **2020**, *27*, 107–115.
3. Xie, Z.; Jiao, J.; Yang, K.; Zhang, H. A state-of-art review on the water-lubricated bearing. *Tribol. Int.* **2023**, *180*, 108276.
4. Zhang, Z.; Ouyang, W.; Liang, X.; Yan, X.; Yuan, C.; Zhou, X.; Guo, Z.; Dong, C.; Liu, Z.; Jin, Y.; et al. Review of the evolution and prevention of friction, wear, and noise for water-lubricated bearings used in ships. *Friction* **2023**, *12*, 1–38.
5. Ouyang, W.; Cheng, Q.; Jin, Y.; Liu, Q.; Wang, B.; Wang, L. Lubrication performance distribution of large aspect ratio water-lubricated bearings considering deformation and shaft bending. *Tribol Trans.* **2021**, *64*, 730–743.
6. Avishai, D.; Morel, G. Experimental investigation of lubrication regimes of a water-lubricated bearing in the propulsion train of a marine vessel. *J. Tribol.* **2021**, *143*, 1–35.
7. Litwin, W.; Dymarski, C. Experimental research on water-lubricated marine stern tube bearings in conditions of improper lubrication and cooling causing rapid bush wear. *Tribol. Int.* **2016**, *95*, 449–455.
8. Patir, N.; Cheng, H.S. Application of average flow model to lubrication between rough sliding surfaces. *J. Lubr. Technol.-Trans. Asme* **1979**, *101*, 220–230.
9. Greenwood, J.A.; Tripp, J.H. The contact of two nominally flat rough surfaces. *Proc. Inst. Mech. Eng. Part J-J. Eng. Tribol.* **1970**, *185*, 625–634.
10. Liang, X.; Han, M.; He, T.; Cui, L.; Yang, Z.; Ouyang, W. A mixed lubrication deterministic model of an elastic support water-lubricated tilting pad thrust bearing. *Lubricants* **2023**, *11*, 262.
11. Wang, Q.; Shi, F.H.; Lee, S.C. A mixed-lubrication study of journal bearing conformal contacts. *J. Tribol.* **1997**, *119*, 456–461.
12. He, T.; Zou, D.; Lu, X.; Guo, Y.; Wang, Z.; Li, W. Mixed-lubrication analysis of marine stern tube bearing considering bending deformation of stern shaft and cavitation. *Tribol. Int.* **2014**, *73*, 108–116.
13. Xie, Z.; Zhu, W. Theoretical and experimental exploration on the micro asperity contact load ratios and lubrication regimes transition for water-lubricated stern tube bearing. *Tribol. Int.* **2021**, *164*, 107105.

14. Charamis, D.; Nikolakopoulos, P.G. Investigation of cavitated flow in water-lubricated bearings considering surface roughness, thermal, and elastic effects. *Lubricants* **2024**, *12*, 107.

15. Xiang, G.; Yang, T.; Guo, J.; Wang, J.; Liu, B.; Chen, S. Optimization transient wear and contact performances of water-lubricated bearings under fluid-solid-thermal coupling condition using profile modification. *Wear* **2022**, *502–503*, 204379.

16. Xiang, G.; Goltsberg, R.; Etsion, I. Role of intermolecular potential in adhesive wear behaviors for elastic-plastic spherical microcontacts. *Tribol. Int.* **2024**, *199*, 110054.

17. Zhao, Z.; Huang, Q.; Sheng, M. The influence of local wear and contact roughness on mixed lubrication of marine stern bearing with misaligned shaft. *Lubr. Sci.* **2023**, *35*, 498–512.

18. Wang, L.; Pei, S.; Xiong, X.; Xu, H. Investigation of the combined influence of turbulence and thermal effects on the performance of water-lubricated hybrid bearings with circumferential grooves and stepped recesses. *Proc. Inst. Mech. Eng. Part J-J. Eng. Tribol.* **2014**, *228*, 53–68.

19. Du, Y.; Lan, J.; Quan, H.; Sun, C.; Liu, X.; Yang, X. Effect of different turbulent lubrication models on the lubrication characteristics of water-lubricated rubber bearings at a high Reynolds number. *Phys. Fluids* **2021**, *33*, 065118.

20. Lv, F.; Zhang, X.; Ji, C.; Rao, Z. Theoretical and experimental investigation on local turbulence effect on mixed−Lubrication journal bearing during speeding up. *Phys. Fluids* **2022**, *34*, 113104.

21. Liu, G.; Li, M. Experimental study on the lubrication characteristics of water-lubricated rubber bearings at high rotating speeds. *Tribol. Int.* **2021**, *157*, 106868.

22. Qiao, J.; Zhou, G.; Pu, W.; Li, R.; He, M. Coupling analysis of turbulent and mixed lubrication of water-lubricated rubber bearings. *Tribol. Int.* **2022**, *172*, 107644.

23. Sun, J.; Gui, C.L. Hydrodynamic lubrication analysis of journal bearing considering misalignment caused by shaft deformation. *Tribol. Int.* **2004**, *37*, 841–848.

24. Liu, Q.; Ouyang, W.; Cheng, Q.; Li, J.; Cheng, Q.; Li, R. Influences of bidirectional shaft inclination on lubrication and dynamic characteristics of the water-lubricated stern bearing. *Mech. Syst. Signal Process.* **2022**, *169*, 108623.

25. Lv, F.; Jiao, C.; Jia, Q.; Xia, K. Influence of structural and operating parameters on lubrication performance of water-lubricated polymer bearing with journal misalignment. *Lubricants* **2022**, *10*, 336.

26. Yang, T.; Han, Y.; Wang, Y.; Xiang, G. Numerical analysis of the transient wear and lubrication behaviors of misaligned journal bearings caused by linear shaft misalignment. *J. Tribol.* **2022**, *144*, 051801.

27. Xie, Z.; Shen, N.; Zhu, W.; Tian, W.; Hao, L. Theoretical and experimental investigation on the influences of misalignment on the lubrication performances and lubrication regimes transition of water lubricated bearing. *Mech. Syst. Signal Process.* **2021**, *149*, 107211.

28. Liang, X.; Yan, X.; Liu, Z.; Ouyang, W. Effect of perturbation amplitudes on water film stiffness coefficients of water-lubricated plain journal bearings based on cfd-fsi methods. *Proc. Inst. Mech. Eng. Part J-J. Eng. Tribol.* **2019**, *233*, 1003–1015.

29. Zhou, G.; Wang, J.; Han, Y.; Li, J.; Pu, W.; Wei, B. Study on the stiffness and damping coefficients of water-lubricated rubber bearings with multiple grooves. *Proc. Inst. Mech. Eng. Part J-J. Eng. Tribol.* **2016**, *230*, 323–335.

30. Wang, X.; Zhou, L.; Huang, M.; Yue, X.; Xu, Q. Numerical investigation of journal misalignment on the static and dynamic characteristics of aerostatic journal bearings. *Measurement* **2018**, *128*, 314–324.

31. Xiang, G.; Wang, Y.; Wang, C.; Lv, Z. Numerical study on the dynamic characteristics of water-lubricated rubber bearing under asperity contact. *Ind Lubr Tribol.* **2021**, *73*, 572–580.

32. Feng, H.; Jiang, S.; Ji, A. Investigations of the static and dynamic characteristics of water-lubricated hydrodynamic journal bearing considering turbulent, thermohydrodynamic and misaligned effects. *Tribol. Int.* **2019**, *130*, 245–260.

33. Ouyang, W.; Liu, Q.; Cheng, Q.; Wan, G.; Jin, Y. Identification of distributed dynamic characteristics of journal bearing with large aspect ratio under shaft bending. *J. Mar. Sci. Eng.* **2022**, *10*, 658.

34. Wu, C.W.; Zheng, L.Q. An average reynolds-equation for partial film lubrication with a contact factor. *J. Tribol.* **1989**, *111*, 188–191.

35. Ng, C.W.; Pan, C. A linearized turbulent lubrication theory. *J. Basic Eng.* **1965**, *87*, 685.

36. Dobrica, M.B.; Fillon, M.; Maspeyrot, P. Mixed elastohydrodynamic lubrication in a partial journal bearing—Comparison between deterministic and stochastic models. *J. Tribol.* **2006**, *128*, 778–788.

37. Mokhtar, M.O.A.; Howarth, R.B.; Davies, P.B. The behavior of plain hydrodynamic journal bearings during starting and stopping. *Asle Trans.* **1977**, *20*, 183–190.

38. Cui, S.; Gu, L.; Wang, L.; Xu, B.; Zhang, C. Numerical analysis on the dynamic contact behavior of hydrodynamic journal bearings during start-up. *Tribol. Int.* **2018**, *121*, 260–268.

39. Liu, Z. Research on Dynamic Characteristic of a Rotor Water Lubricated Rubber Bearing System. Master Thesis, Harbin Institute of Technology, Harbin, China, 2013.